Orbital-resolved calculations of two-center interferences in linear triatomic molecules

Kyle A. Hamer,[1] Daniel R. Tuthill,[2] Timothy D. Scarborough,[2] Louis F. DiMauro,[2] Kenneth Lopata,[3,4] Kenneth J. Schafer,[1] Mette B. Gaarde,[1] and François Mauger[1]

[1]*Department of Physics and Astronomy, Louisiana State University, Baton Rouge, Louisiana 70803, USA*
[2]*Department of Physics, The Ohio State University, Columbus, Ohio 43210, USA*
[3]*Department of Chemistry, Louisiana State University, Baton Rouge, Louisiana 70803, USA*
[4]*Center for Computation and Technology, Louisiana State University, Baton Rouge, Louisiana 70803, USA*

(Received 8 July 2021; accepted 10 September 2021; published 22 September 2021)

We perform *ab initio* calculations of high-harmonic spectroscopy (HHS) of two-center interference phenomena in oriented carbon-dichalcogen molecules, using time-dependent density functional theory (TDDFT). We show that by resolving the harmonic response into contributions from individual Kohn-Sham orbitals, we can extract target-specific characteristics for both the spectral amplitude and phase. We also discuss that this extraction is predicated on a careful analysis and normalization of the harmonic spectrum. Finally, we present field-free scattering calculations that mimic the recollision step in high-order-harmonic generation and allow the calculation of recombination dipole matrix elements without explicitly calculating the scattering states of a molecule. We show that the orbital-resolved TDDFT HHS results and results based on our field-free scattering calculations are in very good agreement with each other.

DOI: 10.1103/PhysRevA.104.033114

I. INTRODUCTION

In the last two decades, high-order-harmonic spectroscopy (HHS) has been explored widely as a tool to probe both the structure and dynamics of molecular and solid-state systems [1–11]. Among the most successful applications of HHS has been the characterization of the geometric structure of linear molecules through two-center interference (TCI) studies [12–16]. TCI occurs in the harmonic response of small molecules in which the highest-occupied molecular orbital (HOMO) is predominantly composed of two centers of charge density, and it can be understood within the three-step model for high-order-harmonic generation (HHG) [17,18]: in the rescattering step of the HHG process from aligned molecules, destructive interference between the dipole signal generated from the two charge centers can occur at the (half-)wavelength components of the rescattering electron wave packet that match the effective center separation [12]. As the molecule is rotated away from the laser polarization direction, its effective length as seen by the returning electron wave packet decreases, and this leads to a paraboliclike feature in the angle-dependent amplitude and phase of the harmonic spectrum [13,16].

Complete characterization of a molecular TCI using HHS thus requires access to both the spectral amplitude and phase. In experiments, this can be achieved using the reconstruction of attosecond beating by interference of two-photon transitions (RABBITT) technique [3,16,19–21]. In *ab initio* calculations, however, extracting phase information is complicated by the interference from multiple quantum-path contributions that tend to wash out the target-specific phase information [21–23], and which is not in general practical to remove through full multiscale calculations including phase-matching effects. In several previous experiment-theory collaborations [16,23], we have shown that seeding the ionization step in the HHG process by an attosecond pulse train (APT), timed so as to preferentially select the short-quantum-path contribution to the harmonic yield [24], vastly improves the ability of *ab initio* calculations to extract target-specific information from the spectral amplitude. However, a drawback of substituting the midinfrared (MIR) driven tunnel ionization step with APT-driven near-one-photon ionization is that orbitals below the HOMO are much more likely to contribute to the harmonic yield than is experimentally realistic, and this again complicates the extraction of spectral phase information [23]. Furthermore, several studies have indicated that multiple orbitals are likely to contribute to the harmonic spectrum for driving wavelengths in the near-infrared as opposed to the MIR [25–27]. It would thus be desirable to be able to separate the contribution from different orbitals [28]. We note here that this further raises the question of whether or not "orbitals" should be interpreted as the field-free molecular orbitals. These orbitals are typically discussed in the context of molecular structure and would generally be mixed in the presence of the MIR field.

In this paper, we explore MIR-driven HHS of TCI phenomena in the carbon-dichalcogen family CO_2, CS_2, and CSe_2, using time-dependent density functional theory (TDDFT). TDDFT provides a scalable computational framework for many-electron systems [29] and has been validated against other calculations or experiments in a number of studies related to strong-field ionization [30–32], charge migration [33,34], and HHS [16]. We show that we can extract both

spectral amplitude and phase information from the TDDFT simulation if we isolate the dipole signal from the highest-lying Kohn-Sham channel that contains the TCI structure. This extraction also relies on avoiding interference between multiple overlapping spectral contributions together with a careful processing and normalization of the HHG signal, and we discuss different avenues for doing so. Finally, we present an approach to performing a field-free scattering calculation within the TDDFT framework that mimics the recollision step in the HHG process and that does not require explicitly calculating the scattering states of the molecule. This approach is based on releasing a moving electron wave packet in the potential of the Kohn-Sham ground state and calculating the dipole signal from the ensuing dynamics. By comparing the results from the scattering calculations to HHS results calculated using MIR wavelengths between 1500 and 2000 nm, we get a measure of how reliably the TCI minimum can be extracted from the HHS calculations.

The paper is organized as follows. Section II describes our theoretical and numerical approach, detailing the process of orbital-resolved TDDFT as well as the HHS analysis. Section III presents angle-resolved calculations of spectral amplitudes and phases for the molecular targets of interest, as well as an outline of and results from our scattering calculations. Lastly, in Sec. IV, we provide a summary and discuss the prospects of our results. Unless otherwise stated, atomic units (a.u.) are used throughout the paper.

II. METHODOLOGY

A. TDDFT simulations

We calculate the field-driven TDDFT dynamics by solving the time-dependent Kohn-Sham (KS) equations [29],

$$i\frac{\partial}{\partial t}\psi_k(\vec{r},t) = \left[-\frac{\nabla^2}{2} + v_{\mathrm{KS}}[\rho](\vec{r},t)\right]\psi_k(\vec{r},t), \qquad (1)$$

where $\psi_k(\vec{r},t)$ is the kth KS orbital, as a function of the position $\vec{r} = (x,y,z)$ and time t. The quantity $v_{\mathrm{KS}}[\rho]$ is the KS potential, which is a functional of the one-body density,

$$\rho(\vec{r},t) = \sum_{k=1}^{N} |\psi_k(\vec{r},t)|^2. \qquad (2)$$

For all numerical simulations, we use a local-density approximation (LDA) exchange-correlation potential [35–38], with an average-density self-interaction correction (ADSIC) [39]. Each of the atoms in the target molecule is represented by a pseudopotential described by [40–42].

The TDDFT simulations are performed using OCTOPUS [43,44], a real-space grid-based software package. Our computational geometry is illustrated in Fig. 1(a): we center the target molecule in a rectangular box which is elongated along the direction of the laser polarization. The box is 140 by 70 by 60 a.u. in the x, y, and z directions, respectively, with a grid spacing of 0.3 a.u. in all directions. We impose the molecular alignment, parametrized by the angle θ, by rotating the target inside that box in the xy plane. With these discretization parameters, we ensure that the ground-state energy of the HOMO varies by less than 0.1 eV as we rotate each molecule. Our calculated ionization potentials are

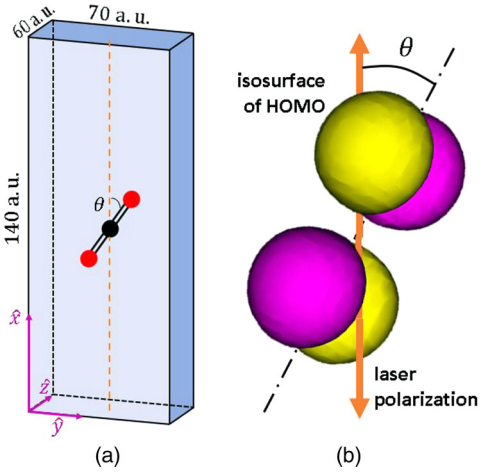

FIG. 1. (a) Schematic of the geometry we use in TDDFT simulations. At the center of the elongated box lies the linear triatomic molecule, which is tilted at an angle θ with respect to the polarization of the driving laser field. (b) Isosurface of the highest-occupied molecular orbital (HOMO) of CO_2, aligned at an angle θ with respect to the laser polarization.

$I_p = 14.5$ eV (experimental 13.8 eV) for CO_2, $I_p = 10.4$ eV (10.1 eV) for CS_2, and $I_p = 9.5$ eV (9.3 eV) for CSe_2 [45]. Note that carbon dichalcogens have a pair of degenerate HOMOs, which can be randomly oriented around the molecular axis. For single-orbital-resolved simulations, we further impose the orientation of the orbitals such that one HOMO lies in the polarization plane while the other is perpendicular to it, such as in Fig. 1(b). We refer to these as the in-plane and out-of-plane orbitals, respectively.

We initialize all our HHG simulations in the DFT molecular ground state, which we compute using the OCTOPUS self-consistent-field iteration routine. To drive HHG, we use a linearly polarized MIR laser field with an envelope which has a two-cycle $\sin^2$ ramp-up and then a constant amplitude. For some of the calculations shown below, we add a weak APT ionization seed to select the short trajectory contribution to the spectrum [23,24]. The APT used here is comprised of odd harmonics, from the 9th to the 17th orders, and is synchronized such that its peak is 0.06 cycles after the peak of the MIR. We systematically match the APT and the MIR polarizations, and scale the APT intensity to 2% of that of the MIR. Note that orbital-resolving HHG spectra allow us to somewhat relax the constraints on the ionization-seed energy components discussed in [23] and potentially have more than just the HOMO being near ionized by the APT. In all TDDFT simulations, we use the OCTOPUS approximated enforced time-reversal symmetry (AETRS) propagation scheme with a time step of 0.05 a.u.

B. Orbital-resolved HHG

We next outline how one can orbital resolve the contributions to the HHG spectrum. Given that the one-body density of Eq. (2) is the sum of the density from the individual Kohn-Sham orbitals, the total dipole moment can also be written as

a sum of single-orbital dipole contributions,

$$d(t) = \iiint x\,\rho(\vec{r},t)\,d\vec{r} = \sum_{k=1}^{N} d_k(t) = \sum_{k=1}^{N} \iiint x|\psi_k(\vec{r},t)|^2\,d\vec{r}. \quad (3)$$

For simplicity, in this paper, we focus on the dipole component that is parallel to the laser polarization axis x. One can easily generalize this analysis to the perpendicular direction, or to the total dipole signal as is done in [23].

The right-hand side of Eq. (3) shows that the total TDDFT dipole signal corresponds to the sum of the dipoles from each individual Kohn-Sham orbital. We use this decomposition to orbital resolve our HHS simulations, by selecting the contributions $d_k(t)$ from the Kohn-Sham orbital(s) of interest. With OCTOPUS, we calculate $d_k(t)$ by exporting the transversely integrated densities $\rho_k(x,t)$ every 0.25 a.u. and then postprocess each dipole component as

$$d_k(t) = \int x \underbrace{\iint |\psi_k(x,y,z,t)|^2\,dy\,dz}_{\rho_k(x,t)}\,dx. \quad (4)$$

C. HHG spectral analysis

Together with orbital resolution, a key element to the success of our HHS computations is the proper processing of the dipole signals. Indeed, one of the main difficulties for HHS simulations is the presence of multiple contributions that add up coherently in the dipole signal of Eq. (4) and that can therefore interfere. Within each half-laser cycle, these correspond to the short- and long-quantum-path trajectories. Over multiple laser cycles, these correspond to the different sets of short and long trajectories from each successive half-laser cycle. At the MIR wavelengths and laser intensities we consider in this paper, the quiver radius is comparable to the radius of our simulation box, such that long trajectories are naturally suppressed by the absorbing boundary conditions [46]; see the movie in the Supplemental Material [47]. For computations where this is not possible, one can instead select the short-trajectory component by using the APT ionization seed discussed above. To avoid the interference between multiple sets of short trajectories, we use a time window that isolates the contribution from an individual half-laser cycle. This short time window also yields a continuous HHG spectrum that is ultimately better suited for our spectroscopic goals here.

Specifically, for our spectral analyses, we combine a high-pass frequency filter F with a half-cycle time window W,

$$\mathrm{HHG}_k(\nu) = \mathcal{F}[W(t)\times\tilde{d}_k(t)](\nu), \quad \tilde{d}_k(t) = [F * d](t), \quad (5)$$

where ν is the HHG frequency and $*$ denotes the convolution operator. We choose a high-pass filter F with a cutoff frequency $\omega_c = 20$ eV set slightly above the ionization threshold of CO_2. It removes intense low-frequency components in the dipole signal that would bleed into higher frequencies when we apply the short time-selection window W. For W, we use a $\cos^4$ function which is centered around the recollision time of the first set of short trajectories in the constant-envelope part of the MIR field, and which lasts one half-laser cycle. We have checked that our HHS results are robust with respect to minor changes in the timing of W and the cutoff frequency ω_c, provided that the harmonic plateau is not significantly dampened by the high-pass filter.

TDDFT HHG spectra contain the target-specific features associated with the carbon-dichalcogen TCI, alongside generic contributions that we would like to get rid of. In the quantitative rescattering (QRS) formalism, the complex HHG spectrum is factorized as [48–51]

$$\mathrm{HHG}_k(\theta,\nu) = \underbrace{\sqrt{I(\theta)}}_{\text{Ion.}}\,\underbrace{\mathrm{HHG}_{\mathrm{ref}}(\nu)}_{\text{Prop.}}\,\underbrace{\mathrm{RDME}_k(\theta,\nu)}_{\text{Scat.}}. \quad (6)$$

The target-specific recombination dipole matrix elements $\mathrm{RDME}_k = \sqrt{\sigma_k}e^{i\phi_k}$ are then characterized by the dipole scattering cross section σ_k and phase ϕ_k. In Eq. (6), $I(\theta)$ is a global ionization-yield factor that only depends on molecular alignment and which we estimate as

$$I(\theta) = \int_{\text{plateau}} |\mathrm{HHG}(\theta,\nu)|^2\,d\nu, \quad (7)$$

where "plateau" corresponds to the portion of the spectrum between the 33rd harmonic order and the cutoff. $\mathrm{HHG}_{\mathrm{ref}}$ is the generic component of the HHG signal, which only depends on the target's ionization potential and the laser's wavelength and intensity. We cancel it out and ultimately access the target-specific scattering cross section σ_k and phase ϕ_k, by normalizing Eq. (6) with a reference HHG spectrum. For instance, the normalization procedure for the phase is [16,23]

$$\phi_k(\theta,\nu) = \mathrm{Arg}\left\{\frac{\mathcal{F}[W\times\tilde{d}_k(\theta)](\nu)}{\mathcal{F}[W\times\tilde{d}_{k,\mathrm{ref}}](\nu)}\right\}, \quad (8)$$

where $\tilde{d}_{k,\mathrm{ref}}(\nu)$ is a reference dipole signal computed for the same target and with the same MIR laser, plus the APT ionization seed if any [23,52]. The target-specific group delay then reads

$$\mathrm{GD}_k(\theta,\nu) = -\frac{\partial}{\partial\nu}\phi_k(\theta,\nu). \quad (9)$$

In all figures, we use the 60-degree HHG signal as the reference. We have checked that its cross section σ and phase ϕ are essentially flat in the range of spectral energies that we are interested in here, which makes it suitable for normalization. Note that one could also use the 90-degree signal for reference.

III. RESULTS

We now move on to the analysis of HHG signals in the carbon-dichalcogen family. Figure 2 shows the results of the orbital-resolved, normalized HHG spectral intensity of the TCI in CO_2 for different laser parameters. Here we treat the two degenerate highest-lying KS channels on an equal footing and coherently add their dipole signal contributions. Figures 2(a)–2(c), in particular, show that for two different wavelengths ($\lambda = 1500$ and 2000 nm) and two different intensities ($I_\circ = 20$ and 60 TW/cm^2), we are able to resolve a clear and consistent TCI minimum with a zero-degree energy

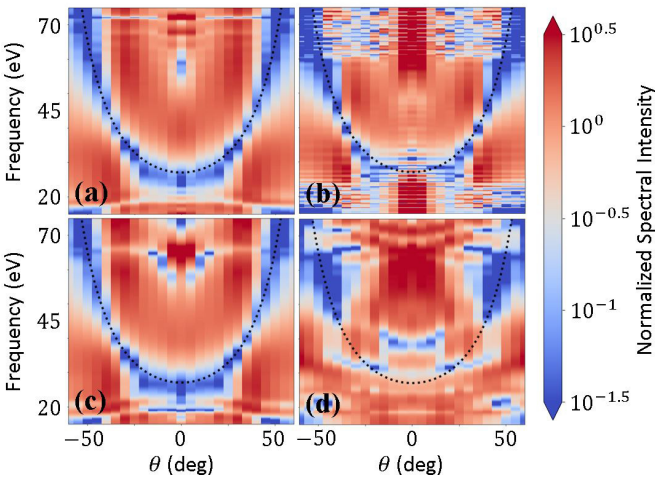

FIG. 2. Normalized angle-resolved high-harmonic spectral intensities for CO_2 calculated from the combined HOMO-resolved dipole signal for different laser parameters: (a) $\lambda = 2000$ nm, $I_\circ = 60$ TW/cm^2, IR only; (b) $\lambda = 2000$ nm, $I_\circ = 20$ TW/cm^2, IR only; (c) $\lambda = 1500$ nm, $I_\circ = 60$ TW/cm^2, IR only; and (d) $\lambda = 1500$ nm, $I_\circ = 60$ TW/cm^2, IR+APT. The black dotted trend lines come from scattering simulations—see Fig. 6.

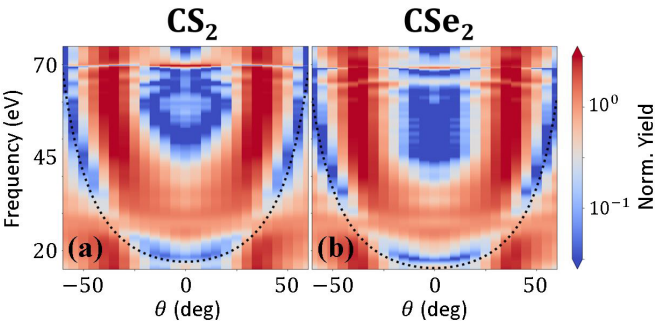

FIG. 3. Normalized angle-resolved high-harmonic spectral intensities for (a) CS_2 and (b) CSe_2 calculated from the IR-only HOMO-resolved dipole signal, using the laser parameters $\lambda = 2000$ nm, $I_\circ = 60$ TW/cm^2 as in Fig. 2(a). Black dotted lines again correspond to scattering simulations.

around 27 eV. The guiding dashed lines are calculated using scattering simulations, which we explain in detail below. In Fig. 2(b), the relatively weak field intensity puts the cutoff around 40 eV. Clearly, this panel shows that our spectral analysis can still resolve the TCI signal in the cutoff region where the signal dies off rapidly. Ultimately, we reach the noise floor at about 60 eV.

In Fig. 2(d), which uses the same wavelength and intensity as Fig. 2(c), we show the effect of adding in an APT ionization seed, as described in the previous section. Overall, the addition of the APT leads to a more complicated angle-dependent target-specific spectral response: While the overall parabolic shape of the IR-only TCI minimum can still be recognized, it occurs at substantially higher energy for small angles. This is unique to CO_2 and we do not observe substantially different TCI features with the other carbon-dichalcogen simulations (not shown). We interpret this reshaping of the TCI feature as resulting from field-induced effects where, in the time-dependent KS channels, the APT couples the HOMO to other state(s). Beyond the static TCI features that we focus on in this paper, this illustrates the potential for extending our spectral analysis to dynamical features as well.

Figure 3 shows the target-specific TCI feature for two other members of the carbon-dichalcogen family: (a) CS_2 and (b) CSe_2. The laser and simulation parameters are identical to those used in Fig. 2(a). Comparing the CO_2, CS_2, and CSe_2 results in the two figures, we see that the TCI minimum has a zero-degree energy which decreases across the family—see, also, more detailed results in Fig. 5. This trend is expected as the carbon-chalcogen bond length increases with heavier elements, and the energy of the TCI feature is expected to qualitatively scale as the inverse of the charge-separation distance squared [53,54]. Quantitative deviations from the plane-wave scattering prediction for the TCI are attributed to the Coulomb tail and target-specific potentials for each compound [16,48,51].

Figures 4(a)–4(c) shows the orbital-resolved, target-specific spectral phase from Eq. (8) for the combined HOMO-resolved dipole signal from each of the three molecular targets. In all panels, we see a clear difference between the value of the phase above and below the TCI. Since the TCI results from destructive interference, it is accompanied by a π phase jump [23]. This transition, as a function of orientation angle θ, is entirely consistent with the features shown in Figs. 2(a) and 3, in that the intensity and phase features overlap; compare, for instance, the dotted lines in both plots. Figure 4(d) shows the group delay for CS_2, calculated from the spectral phase in Fig. 4(b) via Eq. (9). The group delay is what would be measured in a RABBITT experiment and here it consistently exhibits a "dip" at the position of the angle-dependent TCI minimum. The dip is consistent with recent HHS measurements in CO_2 at MIR wavelengths [16].

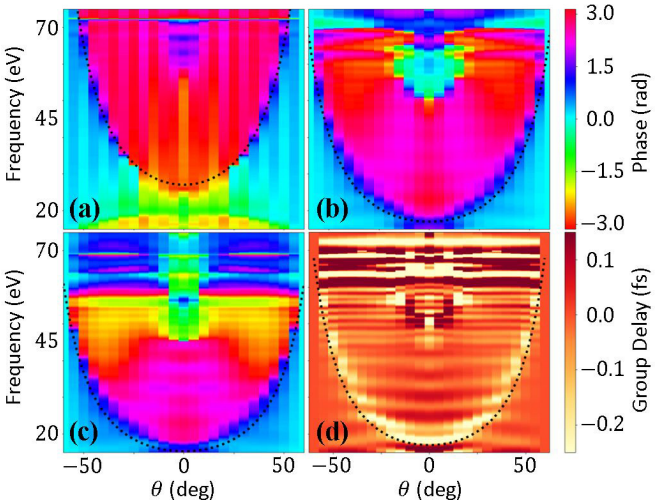

FIG. 4. (a)–(c) Angle-dependent target-specific phases for CO_2, CS_2, and CSe_2, respectively, using the laser parameters $\lambda = 2000$ nm and $I_\circ = 60$ TW/cm^2. (d) The target-specific group delay for CS_2, calculated from the phase in (b). Black dotted lines again correspond to scattering simulations.

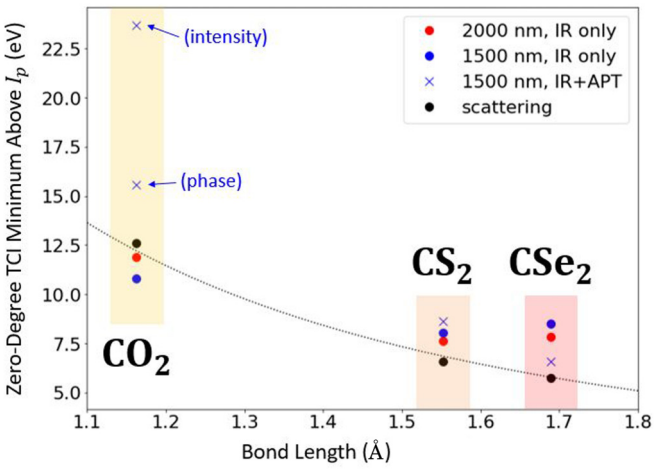

FIG. 5. Markers: comparison of the TCI minimum in the carbon-dichalcogen family for different MIR wavelengths and intensities, as well as scattering simulations; see legend. For each datum, we report the difference between the HHG energy at which the TCI minimum is located at zero degrees and the molecule's ionization potential. The dotted curve is proportional to $1/R^2$, as predicted by scattering theory [53,54].

In the calculations, we do not always find a consistent shape of the group delay feature, in part because we are by construction extracting the phase signal from the part of the spectrum that has very low signal. For example, in CO_2, the direction of the π phase jump is different at small and at large angles [see Fig. 4(a)], and the group delay feature correspondingly changes from a peak to a dip (not shown).

We next return to the question of whether the extraction of the TCI minimum is complicated by field-induced effects, particularly by the addition of the APT. To this end, Fig. 5 shows the location of the zero-degree minima for the three molecules, plotted versus the carbon-chalcogen bond length R, for a number of different pulse parameters. The location has been extracted from the spectra as the energy of the deepest minimum of the zero-degree spectral intensity. We also show the location of the minimum extracted from a scattering calculation (see below) as well as a fit proportional to $1/R^2$, which is what one would expect for plane-wave scattering of the returning electron wave packet on two centers separated by a distance R [16,53,54]. The small variation between the different IR-only extracted results, as well as the good agreement with the scattering results, gives us a measure of the accuracy of the HHS-based approach. The APT-seeded results for CS_2 and CSe_2 also agree well with the other results, whereas for CO_2, the APT-seeded results are substantial outliers. Taken together, these results illustrate the benefits of comparing spectral features across multiple dimensions [52,55]—here, the laser fields and the carbon-dichalcogen family—to identify both generic spectroscopic features that can be compared against each other and signatures that are unique to a system.

A general caveat to the procedure we propose here is that the KS orbitals of Eq. (1) are not physical quantities and thus our orbital-resolved HHS signals do not exactly correspond to experimental observables. However, we expect that our approach does compensate for some of the known inaccuracies in the total HHS signal due to the use of various approximations. Compared to single-active-electron or static-orbital approximations, we expect time-dependent KS orbitals to provide significant improvements by allowing for (i) laser-field dressing effects such as polarization, Stark shift, reshaping of the density, etc., which can qualitatively affect the HHS response [23,54]; and (ii) multichannel contributions, if more than one KS channel significantly contributes to the HHG signal and is included in the analysis. In that sense, we expect time-dependent KS orbitals to reproduce some elements of fully correlated models, although the qualitative and quantitative agreement is likely to be both system and observable dependent [5,50].

Next, we explore the QRS formalism of Eq. (6) in more detail, both for its own sake and to better understand when field-dependent effects are important. For this, we need the target-specific scattering cross section σ and phase ϕ that compose the RDME, which is defined in terms of field-free molecular and scattering wave functions. As such, the RDME can be seen as corresponding to the normalized HHS spectrum in the limit of vanishing laser intensity, where field-induced effects disappear, while keeping the ponderomotive energy constant, something that would require performing HHS calculations at longer and longer wavelengths. In this section, we sidestep these complications and calculate the RDME numerically with a field-free time-dependent wave packet calculation. In particular, we propagate, in the target's DFT potential, a scattering electron wave packet from which we extract the RDME without explicitly computing any scattering states [56], which is a nontrivial process for arbitrary potentials.

Our scattering simulations rely upon the idea that the asymptotic shape of scattering wave functions ψ_{scat} is identical for all potentials with a Coulomb tail. This means that we can formally decompose a wave packet ψ_{seed} initially localized away from the core as

$$\psi_{\text{seed}}(\vec{r}, t=0) \approx \int w(\vec{p})\, \psi_{\text{scat}}[\theta, \vec{p}](\vec{r})\, d\vec{p}, \tag{10}$$

with $\vec{p}$ labeling the asymptotic scattering momentum. In the factorization, the weight distribution $w(\vec{p})$ is solely determined by ψ_{seed}, while all of the information associated with the specifics of the molecular target and its alignment are contained in the scattering states ψ_{scat}. In a practical sense, for the scattering simulations, we know the initial scattering seed $\psi_{\text{seed}}(\vec{r}, t=0)$ and seek to cancel out the weights $w(\vec{p})$ in order to access the scattering dipole matrix elements $\langle \psi_{\text{scat}} | \hat{x} | \psi_k^{\text{MO}} \rangle = \text{RDME}_k$ of Eq. (6) without ever explicitly computing $w(\vec{p})$ or ψ_{scat}.

From the wave packet expansion of Eq. (10), we formally write the time-dependent dipole between the field-free propagation of the scattering seed ψ_{seed} and a molecular orbital ψ_k^{MO} as

$$\begin{aligned} d_k^{\text{sc}}(\theta, t) &= \langle \psi_{\text{seed}}(t) | \hat{x} | \psi_k^{\text{MO}}(t) \rangle \\ &= \int w(\vec{p}) \langle \psi_{\text{scat}}(\theta, \vec{p}) | \hat{x} | \psi_k^{\text{MO}}(0) \rangle e^{i(I_p^{(k)} + \frac{|\vec{p}|^2}{2})t}\, d\vec{p} \\ &\quad + \text{c.c.}, \end{aligned} \tag{11}$$

where $I_p^{(k)}$ is the ionization potential of the kth molecular orbital and c.c. denotes the complex conjugate. In this equation, we have used the fact that the scattering-state energy is related to the asymptotic momentum through $E = |\vec{p}|^2/2$. Note that the term $w(\vec{p})\langle\psi_{\rm scat}(\theta, \vec{p})|\hat{x}|\psi_k^{\rm MO}(0)\rangle$ is time independent, and thus the scattering dipole signal $d_k^{\rm sc}$ is explicitly written as a Fourier expansion at the frequencies $I_p^{(k)} + |\vec{p}|^2/2$. In other words, the Fourier transform of this scattering dipole is proportional to the RDME,

$$\mathcal{F}\big[d_k^{\rm sc}(\theta, t)\big](\nu) \propto {\rm RDME}_k(\theta, \nu), \tag{12}$$

with $\nu = I_p^{(k)} + |\vec{p}|^2/2$. The only unknown factor is the proportionality coefficient $w(\vec{p})$, which we remove by normalizing the scattering-seed results with a reference angle $\mathcal{F}[W^{\rm sc} \times d^{\rm sc}(\theta)]/\mathcal{F}[W^{\rm sc} \times d^{\rm sc}(\theta_{\rm ref})]$, like we did in the TDDFT simulations above. Here, $W^{\rm sc}$ is a broad time window equal to 1 for most of the scattering simulation and going gently to zero, with a $\cos^6$ shape, at the end of the simulation time.

Our computational approach to the scattering simulations is similar to that described in Sec. II A. We put the carbon-dichalcogen target at the origin of the simulation box and impose alignment by rotating the molecule inside the box; see, again, Fig. 1(a). In all simulations, we use an initial scattering seed of the form

$$\psi_{\rm seed}(\vec{r}, t = 0) = \mathcal{N}_\parallel(x - x_0, y)\mathcal{N}_\perp(z)e^{ip_0 x}, \tag{13}$$

with central position $x_\circ = -60$ a.u. and momentum $\vec{p}_\circ = 1.21$ a.u. ($\approx$20 eV). The in-plane component $\mathcal{N}_\parallel$ is a constant in the y direction and a Gaussian function in the x direction, such that $\mathcal{N}_\parallel e^{ip_\circ x}$ emulates the wave front, along the scattering direction, of the rescattering electron in HHG. For convenience, we choose the transverse out-of-plane component of the scattering seed $\mathcal{N}_\perp$ to match the symmetry of the target molecular orbital, i.e., its shape reflects the symmetry of the outgoing wave packet resulting from strong-field ionization, or one-photon ionization with the APT seed. For instance, for the out-of-plane HOMO of Fig. 1(b), we take $\mathcal{N}_\perp(z) = (L_z/2\pi)\sin(2\pi z/L_z)$, where L_z is the total length of the simulation box in the direction of the lobes of the Π orbital. $\mathcal{N}_\perp$ is then the lowest box mode of the correct symmetry supported by the simulation domain.

In the scattering simulations, we time propagate $\psi_{\rm seed}$ in the DFT ground-state potential $v_{\rm KS}$, which we export from OCTOPUS, using a second-order spectral-split scheme with a time step of 0.01 a.u. for about 3 fs. With our box and initial-seed parameters, this ensures that the entire scattering wave packet can travel through the target. To enhance the signals' spectral resolution, in the computation of the scattering dipole components we artificially shift the molecular orbital's ionization potential to a higher energy value, which we then compensate for in Eq. (12). Spatially, we use a rectangular domain elongated along the scattering direction x, similar to Fig. 1(a). We impose absorbing boundary conditions [57] in the scattering direction and periodic boundary conditions in the other directions (y and z). On both ends of the domain, we leave a buffer of about 40 a.u. along, and 30 a.u. transversely to, the scattering direction between the faces of the box and the centers of both the molecule and the initial ionization seed. Finally, we use the same 0.3 a.u. discretization step in all directions as for TDDFT simulations.

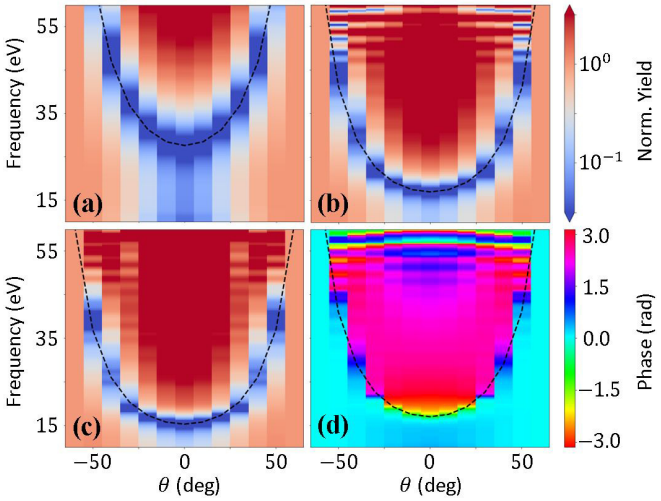

FIG. 6. Field-free scattering simulations, for the out-of-plane HOMO, in the carbon-dichalcogen family. (a)–(c) The angle-resolved target-specific intensity σ_k^2 for CO_2, CS_2, and CSe_2, respectively. (d) The corresponding phase ϕ_k for CS_2.

In Fig. 6, we show the results of the scattering simulations described above for the out-of-plane HOMO in the carbon-dichalcogen family. Overall, these are strikingly similar to the TDDFT MIR-only HHS results with a clear local minimum in the spectral intensity that moves to higher energies with increasing the alignment angle; compare the dashed curves with Figs. 2(a)–2(c) and 3. The scattering phase in Fig. 6(d) is also in very good agreement with the HHS results of Fig. 4(b). Note that for small alignment angle, the CS_2 TCI feature is close to the ionization threshold and it is therefore more challenging to accurately extract the phase information, which explains the small strip of negative phase around 20 eV in Fig. 6(d).

IV. CONCLUSION

In summary, we have shown that we can reliably recover both the amplitude and phase information specific to a molecular target in TDDFT HHG simulations. To do so, we have combined orbital resolving the dipole signal with careful signal processing and normalization. We compared generic strategies to do so, including how to select a single set of short trajectories either through the simulation-box absorbing boundary conditions [46] or with an APT-ionization seed [24], together with a well-timed short-window time filtering. We also discussed field-induced effects that can be unique to a specific target, such as the reshaping of the TCI feature induced by the APT dressing in CO_2 and that is absent in the other carbon dichalcogens. Finally, we have introduced a simple method to numerically approximate the field-free scattering-dipole matrix elements through coherent scattering simulations. These field-free scattering simulations showed an excellent agreement when compared to the full TDDFT HHS results.

The feasibility of using the absorbing boundary conditions versus the APT-ionization seed for selecting the short-trajectory contributions can be strongly limited by the

specifics of the problem at hand. That said, we can draw some generic pros and cons to each approach. For the former, the obvious pro is that it is the closest to experimental conditions since no additional laser field is added to the simulations. This means that one can expect the wavelength- and intensity-dependent ionization factor in Eq. (6) to be relatively well accounted for, especially for KS channels that are close to each other energetically. For instance, in our simulations, this has enabled us to combine the dipole signals from the two degenerate highest-lying KS channels while, with the APT, we observed the "best" results when further selecting the out-of-plane signal only (not shown). On the other hand, the absorbing boundary conditions must essentially leave the short-trajectory component intact while damping the long one without inducing spurious reflections. Simultaneously fulfilling these two conditions can become increasingly difficult for shorter (than MIR) wavelengths. Also, the performance of the absorbing-boundary approach for multicycle studies is unclear. For the APT, in addition to the difficulty of (re)combining the dipole signal from different KS channels, the performance of the ionization seed is dependent upon a proper calibration of the APT. This includes avoiding APT-field-induced effects, and there are no one-size-fits-all solutions. One clear advantage of the APT-seed approach, though, is that it can clearly be extended to multicycle studies since it is synchronized to the driving field.

ACKNOWLEDGMENTS

This work was supported by the U.S. Department of Energy, Office of Science, Office of Basic Energy Sciences, under Award No. DE-SC0012462. Portions of this research were conducted with high performance computational resources provided by Louisiana State University and the Louisiana Optical Network Infrastructure [58].

[1] J. Itatani, J. Levesque, D. Zeidler, H. Niikura, H. Pépin, J. C. Kieffer, P. B. Corkum, and D. M. Villeneuve, Nature (London) **432**, 867 (2004).
[2] S. Patchkovskii, Z. Zhao, T. Brabec, and D. M. Villeneuve, Phys. Rev. Lett. **97**, 123003 (2006).
[3] S. Haessler, J. Caillat, W. Boutu, C. Giovanetti-Teixeira, T. Ruchon, T. Auguste, Z. Diveki, P. Breger, A. Maquet, B. Carré, R. Taïeb, and P. Salières, Nat. Phys. **6**, 200 (2010).
[4] C. Vozzi, M. Negro, F. Calegari, G. Sansone, M. Nisoli, S. de Silvestri, and S. Stagira, Nat. Phys. **7**, 822 (2011).
[5] O. Smirnova, Y. Mairesse, S. Patchkovskii, N. Dudovich, D. Villeneuve, P. Corkum, and M. Y. Ivanov, Nature (London) **460**, 972 (2009).
[6] R. M. Lock, S. Ramakrishna, X. Zhou, H. C. Kapteyn, M. M. Murnane, and T. Seideman, Phys. Rev. Lett. **108**, 133901 (2012).
[7] M. C. H. Wong, A.-T. Le, A. F. Alharbi, A. E. Boguslavskiy, R. R. Lucchese, J.-P. Brichta, C. D. Lin, and V. R. Bhardwaj, Phys. Rev. Lett. **110**, 033006 (2013).
[8] J. P. Marangos, J. Phys. B **49**, 132001 (2016).
[9] P. M. Kraus and H. J. Wörner, Angew. Chem., Intl. Ed. **57**, 5228 (2018).
[10] T. T. Luu and H. J. Wörner, Nat. Commun. **9**, 916 (2018).
[11] M. R. Bionta, E. Haddad, A. Leblanc, V. Gruson, P. Lassonde, H. Ibrahim, J. Chaillou, N. Émond, M. R. Otto, B. J. Siwick, M. Chaker, and F. Légaré, Tracking ultrafast solid-state dynamics in VO2 using high harmonic spectroscopy, in *The 22nd International Conference on Ultrafast Phenomena 2020*, edited by F. Kärtner, M. Khalil, R. Li, F. Légaré, and T. Tahara (Optical Society of America, 2020), p. Th3B.7.
[12] T. Kanai, S. Minemoto, and H. Sakai, Nature (London) **435**, 470 (2005).
[13] C. Vozzi, F. Calegari, E. Benedetti, J.-P. Caumes, G. Sansone, S. Stagira, M. Nisoli, R. Torres, E. Heesel, N. Kajumba, J. P. Marangos, C. Altucci, and R. Velotta, Phys. Rev. Lett. **95**, 153902 (2005).
[14] K. Kato, S. Minemoto, and H. Sakai, Phys. Rev. A **84**, 021403(R) (2011).
[15] A. Rupenyan, P. M. Kraus, J. Schneider, and H. J. Wörner, Phys. Rev. A **87**, 031401(R) (2013).
[16] T. T. Gorman, T. D. Scarborough, P. M. Abanador, F. Mauger, D. Kiesewetter, P. Sándor, S. Khatri, K. Lopata, K. J. Schafer, P. Agostini, M. B. Gaarde, and L. F. DiMauro, J. Chem. Phys. **150**, 184308 (2019).
[17] P. B. Corkum, Phys. Rev. Lett. **71**, 1994 (1993).
[18] K. J. Schafer, B. Yang, L. F. DiMauro, and K. C. Kulander, Phys. Rev. Lett. **70**, 1599 (1993).
[19] H. G. Muller, Appl. Phys. B **74**, s17 (2002).
[20] W. Boutu, S. Haessler, H. Merdji, P. Breger, G. Waters, M. Stankiewicz, L. J. Frasinski, R. Taieb, J. Caillat, A. Maquet, P. Monchicourt, B. Carre, and P. Salieres, Nat. Phys. **4**, 545 (2008).
[21] S. B. Schoun, A. Camper, P. Salières, R. R. Lucchese, P. Agostini, and L. F. DiMauro, Phys. Rev. Lett. **118**, 033201 (2017).
[22] M. Labeye, F. Risoud, C. Leveque, J. Caillat, A. Maquet, T. Shaaran, P. Salières, and R. Taïeb, Phys. Rev. A **99**, 013412 (2019).
[23] F. Mauger, P. M. Abanador, T. D. Scarborough, T. T. Gorman, P. Agostini, L. F. DiMauro, K. Lopata, K. J. Schafer, and M. B. Gaarde, Struct. Dyn. **6**, 044101 (2019).
[24] K. J. Schafer, M. B. Gaarde, A. Heinrich, J. Biegert, and U. Keller, Phys. Rev. Lett. **92**, 023003 (2004).
[25] B. K. McFarland, J. P. Farrell, P. H. Bucksbaum, and M. Gühr, Science **322**, 1232 (2008).
[26] H. Akagi, T. Otobe, A. Staudte, A. Shiner, F. Turner, R. Dörner, D. M. Villeneuve, and P. B. Corkum, Science **325**, 1364 (2009).
[27] H. J. Wörner, J. B. Bertrand, P. Hockett, P. B. Corkum, and D. M. Villeneuve, Phys. Rev. Lett. **104**, 233904 (2010).
[28] S. Haessler, J. Caillat, and P. Salieres, J. Phys. B **44**, 203001 (2011).
[29] W. Kohn and L. J. Sham, Phys. Rev. **140**, A1133 (1965).
[30] X. Chu, Phys. Rev. A **82**, 023407 (2010).
[31] A. Sissay, P. Abanador, F. Mauger, M. B. Gaarde, K. J. Schafer, and K. Lopata, J. Chem. Phys. **145**, 094105 (2016).

[32] P. Sándor, A. Sissay, F. Mauger, P. M. Abanador, T. T. Gorman, T. D. Scarborough, M. B. Gaarde, K. Lopata, K. J. Schafer, and R. R. Jones, Phys. Rev. A **98**, 043425 (2018).
[33] P. M. Kraus, B. Mignolet, D. Baykusheva, A. Rupenyan, L. Horný, E. F. Penka, G. Grassi, O. I. Tolstikhin, J. Schneider, F. Jensen, L. B. Madsen, A. D. Bandrauk, F. Remacle, and H. J. Wörner, Science **350**, 790 (2015).
[34] A. S. Folorunso, A. Bruner, F. Mauger, K. A. Hamer, S. Hernandez, R. R. Jones, L. F. DiMauro, M. B. Gaarde, K. J. Schafer, and K. Lopata, Phys. Rev. Lett. **126**, 133002 (2021).
[35] F. Bloch, Z. Phys. **57**, 545 (1929).
[36] P. Dirac, Math. Proc. Cambridge Philos. Soc. **26**, 376 (2008).
[37] J. P. Perdew and A. Zunger, Phys. Rev. B **23**, 5048 (1981).
[38] M. A. Marques, M. J. Oliveira, and T. Burnus, Comput. Phys. Commun. **183**, 2272 (2012).
[39] C. Legrand, E. Suraud, and P.-G. Reinhard, J. Phys. B **35**, 1115 (2002).
[40] N. Troullier and J. L. Martins, Phys. Rev. B **43**, 1993 (1991).
[41] S. G. Louie, S. Froyen, and M. L. Cohen, Phys. Rev. B **26**, 1738 (1982).
[42] J. M. Soler, E. Artacho, J. D. Gale, A. García, J. Junquera, P. Ordejón, and D. Sánchez-Portal, J. Phys.: Condens. Matter **14**, 2745 (2002).
[43] X. Andrade, J. Alberdi-Rodriguez, D. A. Strubbe, M. J. T. Oliveira, F. Nogueira, A. Castro, J. Muguerza, A. Arruabarrena, S. G. Louie, A. Aspuru-Guzik, A. Rubio, and M. A. L. Marques, J. Phys.: Condens. Matter **24**, 233202 (2012).
[44] X. Andrade, D. Strubbe, U. De Giovannini, A. H. Larsen, M. J. T. Oliveira, J. Alberdi-Rodriguez, A. Varas, I. Theophilou, N. Helbig, M. J. Verstraete, L. Stella, F. Nogueira, A. Aspuru-Guzik, A. Castro, M. A. L. Marques, and A. Rubio, Phys. Chem. Chem. Phys. **17**, 31371 (2015).
[45] D. C. Frost, S. T. Lee, and C. A. McDowell, J. Chem. Phys. **59**, 5484 (1973).
[46] Y. P. Li, S. J. Yu, X. Y. Duan, Y. Z. Shi, and Y. J. Chen, J. Phys. B **49**, 075603 (2016).
[47] See Supplemental Material at http://link.aps.org/supplemental/10.1103/PhysRevA.104.033114 for more details.
[48] F. Mauger, P. M. Abanador, K. Lopata, K. J. Schafer, and M. B. Gaarde, Phys. Rev. A **93**, 043815 (2016).
[49] M. V. Frolov, N. L. Manakov, T. S. Sarantseva, and A. F. Starace, J. Phys. B **42**, 035601 (2009).
[50] Z. Chen, A.-T. Le, T. Morishita, and C. D. Lin, Phys. Rev. A **79**, 033409 (2009).
[51] C. D. Lin, A.-T. Le, Z. Chen, T. Morishita, and R. Lucchese, J. Phys. B **43**, 122001 (2010).
[52] D. R. Tuthill, F. Mauger, T. D. Scarborough, R. R. Jones, M. B. Gaarde, K. Lopata, K. J. Schafer, and L. F. DiMauro, J. Mol. Spectrosc. **372**, 111353 (2020).
[53] X. Zhu, Q. Zhang, W. Hong, P. Lan, and P. Lu, Opt. Express **19**, 436 (2011).
[54] A. Etches, M. B. Gaarde, and L. B. Madsen, Phys. Rev. A **84**, 023418 (2011).
[55] T. D. Scarborough, T. T. Gorman, F. Mauger, P. Sándor, S. Khatri, M. B. Gaarde, K. J. Schafer, P. Agostini, and L. F. DiMauro, Appl. Sci. **8**, 1129 (2018).
[56] D. J. Tannor, *Introduction to Quantum Mechanics: A Time-dependent Perspective* (University Science Books, Sausalito, CA, 2007), Chap. 17, pp. 559–578.
[57] R. Kosloff and D. Kosloff, J. Comput. Phys. **63**, 363 (1986).
[58] See Louisiana State University, http://www.hpc.lsu.edu and the Louisiana Optical Network Infrastructure, http://www.loni.org.